Supplementary Information

Unblocking A Rigid Purine MOF for Kinetic Separation of Xylenes

Richelle Lyndon,[a]‡ Yuxiang Wang,[a]‡ Ian M. Walton,[a] Yao Ma,[a] Yang Liu,[a] Zhenzi Yu, [a] Guanghui Zhu,[a] Samuel Berens,[b] Yu-Sheng Chen,[c] SuYin G. Wang,[c] Sergey Vasenkov,[b] David S. Sholl,[a,d] Krista S. Walton,[a] Simon H. Pang,[e] Ryan P. Lively[a]*

AUTHOR ADDRESS

a. School of Chemical & Biomolecular Engineering, Georgia Institute of Technology, 311 Ferst Drive NW, Atlanta, GA 30332, USA

b. Department of Chemical Engineering, University of Florida, Gainesville, FL, 32611, USA.

c. ChemMatCARS Beamline, The University of Chicago, Advanced Photon Source, Lemont, IL 60439, USA.

d. Oak Ridge National Laboratory, Oak Ridge, TN 37830, USA

e. Lawrence Livermore National Laboratory, 7000 East Avenue, Livermore, CA 94550, USA.

Table of Contents

Materials & Synthesis

Materials

All reagents were used without further purification. Zinc bromide dihydrate ($ZnBr_2.2H_2O$, 99%) and zinc iodide (anhydrous, 99.999%) were purchased from Sigma Aldrich. Purine (98 %) was purchased from Combi-Blocks. Chloroform (99.8%) was purchased from VWR. N, N-Dimethylformamide (anhydrous, 99.8%), *para*-xylene (PX, 99%), *ortho*-xylene (OX, 99%), and *meta*-xylene (MX, 99%) were purchased from Alfa Aesar. 1,3,5-Triisopropylbenzene (TIPB) and 1,3,5-tri-tert-butylbenzene (TTBB) was purchased from TCI America. Carbon dioxide (99.999%), methane (UHP), argon (UHP), and helium (UHP) were purchased from Airgas.

Synthesis

Zn(purine)Br

In a 60 mL vial, purine (1.203 g, 10 mmol) was dissolved in 30 mL anhydrous DMF. In a separate vial, $ZnBr_2 \cdot 2H_2O$ (0.522 g, 2 mmol) was dissolved in 10 mL anhydrous DMF. The metal salt solution was added to the purine solution and briefly mixed. The vials were placed in a rotating oven and set to rotate at 40 rpm at 65 °C for 72 h. The reaction mixture was then cooled to room temperature. A Pasteur pipet was used to carefully remove the reaction solution from the vial. The sample was washed with 30 mL fresh DMF and soaked for 3 hours. Afterwards, the sample was solvent exchanged with 30 mL $CHCl_3$ three times for 4 hours. The off-white crystals were dried in ambient conditions.

Zn(purine)I

In a 60 mL vial, purine (1.203 g, 10 mmol) was dissolved in 30 mL anhydrous DMF. In a separate vial, ZnI_2 (0.640 g, 2 mmol) was dissolved in 10 mL anhydrous DMF. The metal salt solution was added to the purine solution and briefly mixed. The vials were placed in a rotating oven and set to rotate at 40 rpm at 65 °C for 72 h. The reaction mixture was then cooled to room temperature. A Pasteur pipet was used to carefully remove the reaction solution from the vial. The sample was washed with 30 mL fresh DMF and soaked for 3 hours. Afterwards, the sample was solvent exchanged with 30 mL $CHCl_3$ three times for 4 hours. The pale-yellow crystals were dried in ambient conditions.

Characterizations

Powder X-Ray Diffraction (PXRD)

PXRD patterns of samples were collected from a X'Pert Pro PANalytical (Malvern Panalytical) diffractometer at 40 kV and 40 mA (Cu Kα source, λ = 1.541 nm). The patterns were collected with a step size of 0.017° 2θ and scan time of 10.16 s/step over 2θ range of 5-50°.

Scanning electron microscopy (SEM)

SEM images were acquired from an SU8230 (Hitachi) field emission scanning electron microscope with an accelerating voltage of 1-2 kV and emission current of 5 μA at a working distance of 7-9 mm. The samples were dispersed onto double-sided conductive copper tape attached to a flat aluminum sample stub. ImageJ was used to analyze the particle size distribution (Fig. S11).

Thermogravimetric Analysis (TGA)

Thermogravimetric analyses of MOF samples were carried out on a TGA Q500 (TA Instruments) with a heating rate of 5 °C/min to 700 °C under nitrogen flow.

Volumetric Gas Sorption Measurement

Single component CO_2 and CH_4 adsorption isotherms of MOF samples at 298 K were measured with ASAP 2020 (Micromeritics) using an equilibration interval of 60 seconds. The equilibration interval refers to time required for the pressure change to be less than 0.01% of the average pressure during equilibration.

Single component Ar adsorption isotherms at 87.3 K were collected on a Micromeritics 3Flex Surface Characterization Analyzer with temperature control accomplished through the use of a Lake Shore 366 Temperature Controller connected to a cryostage by Coldedge Technologies. The samples were evacuated and activated at 200 °C for at least 12 h under vacuum.

Single Crystal X-Ray Crystallography

All SCXRD data were collected at the ChemMatCARS beamline (15-IDD) of the Advanced Photon Source (APS) at Argonne National Laboratory (ANL). Diffraction data was collected with λ=0.41328 Å radiation on a Pilatus 3X CdTe 1M detector. TIFF formatted frames produced from the Pilatus 3XCdTe 1M detector were converted to .srfm files for analysis with the Bruker APEX3 software suite by the use of a conversion program developed at the ChemMatCARS beamline.

Data collected on Zn(purine)Br, structure RS8D3, was collected on a suitable crystal 65 μm along the longest axis. Data was collected in two distinct phi scans, 360° with a 0.5° frame width and a 0.5 second exposure time.

Data collected on Zn(purine)I, structure RS10D1, was collected on a suitable crystal 22 μm along the longest axis. Data was collected in two distinct phi scans, 360° with a 0.5° frame width and a 2 second exposure time.

The crystallographic parameters of both MOFs are shown in Table S1. Both structures were found to from identical lattices with P2$_1$/n symmetry. The void space of the MOFs was found to be one dimensional along the *b*-axis of the unit cell. While the change in the counter ion from bromine to iodine did not result in a significant change to the structure of the MOF, a slight increase in the *a* and *c* vectors, the volume, and the *β* angle of the unit cell accompanied the change in halide counter ion.

Structure Optimization

The purine MOF, an isolated chloroform molecule, and the purine MOF with four adsorbed chloroform molecules were energy minimized using spatially periodic Density Functional Theory calculations performed in the Vienna Ab initio Simulation Package (VASP) with a planewave basis set and core electrons represented with projector augmented wave (PAW) potentials.[1, 2] For all DFT calculations, we use Perdew−Burke−Ernzerhof (PBE) functional and semiempirical dispersion corrections via the DFT-D3 method to better capture van der Waals dispersion interactions within MOFs.[3-5] We use a planewave basis set with a cutoff energy of 600 eV, with total energy and atomic force convergence criteria for energy relaxation of 10^{-5} eV and 0.05 eV/Å. Unit cell parameters from single crystal XRD and from DFT-optimized chloroform-free structure are consistent with each other as shown in the Table S2.

Geometric Analysis

The accessible surface area and pore limiting diameter of MOF structures were characterized with Zeo++.[6] A probe radius of 1.7 Å (corresponding to the Van der Waals radius of Ar) and covalent radii from the Cambridge Crystallographic Data Centre for MOF framework atoms were used.[7]

Adsorption Energy Calculations

DFT calculations were used to estimate the binding energy of chloroform in the MOF. The net binding energies of four adsorbed chloroform molecules was defined by

$$-\Delta E = E_{ads + MOF} - E_{MOF} - 4 \times E_{ads}$$

where $E_{ads+MOF}$, E_{MOF}, and E_{ads} represent the energy of purine MOF with four adsorbed chloroform molecules, the energy of the empty purine MOF, and the energy of a chloroform molecule in the gas phase, respectively. With this definition, ΔE is positive when adsorption energy is exothermic and the binding energy per molecule is $\Delta E/4$. Illustrations of the chloroform molecules inside the MOF's channels from DFT-optimized structures are shown in Fig. S4. This calculation yielded a binding energy per molecule of 0.268 eV.

Gravimetric Sorption Measurements of Xylene Vapor

Single-component gravimetric vapor sorption of *p*-xylene and *o*-xylene in MOFs were measured with a VTI-SA+ automated vapor sorption analyzer (TA Instruments) at a relative pressure ranging from 0.00 to 0.05 at 303.15 K with equilibrium criteria of mass change less than 0.001 wt% in a 45-minute period. Prior to measurements, the MOF samples were heated overnight at 200 °C under vacuum. After that, the MOF samples were then loaded into the instrument and further dried in situ at 110 °C for 48 hours, under flowing nitrogen.

Xylene sorption in Zn(purine)Br cannot be observed. The measured *p*-xylene and *o*-xylene were below 0.01 wt%, which are within the noise and thus, cannot be measured using this method. Xylene sorption in Zn(purine)I can be measured. The obtained uptake change data are first normalized using:[8]

$$\frac{M_t}{M_\infty} = \frac{M(t) - M_0}{M(t = \infty) - M_0} \tag{1}$$

where $M(t)$ is the amount of *p*-xylene or *o*-xylene into Zn(purine)I at time point *t* and $M(t = \infty)$ is the theoretical sorption amount after infinite time. Generally, the experimental kinetic uptake curve can be fitted by a Fickian mass transfer model to determine the transport diffusion coefficient.

The diffusion path of Zn(purine)I is along the *b*-axis, which is assumed to correspond to the longest dimension of the crystals. Bravais−Friedel−Donnay−Harker (BFDH) method was applied for crystal morphology simulation using the Mercury software. While this method is well proven on molecular crystals, the application to MOFs is as yet unclear. The assumption of the *b-axis* corresponding to the longest dimension of the crystal is done under the assumption that the application of the BFDH method to this MOFs is valid. The lattice parameters and atomic coordinates used in the model were obtained from experimentally determined single crystal data. The particle size distribution were obtained *via* SEM and analyzed using the ImageJ software.

Based on above assumption, the kinetic mass uptake processes can be described by the 1D Fickian diffusion model.[8] For a cylindrical particle in adsorbate concentration at its external surface at time zero, the mathematical infinite series solution for the Fickian uptake is given by:[8]

$$\left.\frac{M_t}{M_\infty}\right|_{L_i} = 1 - \sum_{n=0}^{\infty} \frac{8}{(2n+1)^2\pi^2} exp\left[-\frac{D(2n+1)^2\pi^2 t}{4L_i^2} \right]$$
(2)

where t is the diffusion time, L_i is the half-length of the Zn(purine)I particle i, and D is the transport diffusivity.

The apparent Fickian uptake considering particle size distribution can be approximated as the superposition of the solutions for each particle within the population:[9]

$$\left.\frac{M_t}{M_\infty}\right|_{PSD} = \sum_i X_i \left.\frac{M_t}{M_\infty}\right|_{L_i}$$
(3)

where X_i is the volume-weighted fraction of particles with a half-length of L_i and can be obtained from $X_i = V_i \bigg/ \sum_i V_i$. V_i is the volume of particles of a half-length L_i.

Pulsed field gradient – nuclear magnetic resonance (PFG-NMR) spectroscopy

All ^{1}H NMR measurements were performed at 296 ± 1 K on an 89 mm bore 17.6 T Avance III HD 750 MHz spectrometer (Bruker Biospin). 97 mg of Zn(purine)I was loaded into an NMR tube and attached to a custom vacuum manifold. The sample was degassed for around 10 hours overnight at 110 °C and 60 mTorr. Once evacuated, 0.026 mmol of p-xylene vapor was cryogenically loaded into the MOF bed via the vacuum manifold. The sample was then flame sealed, removed from the vacuum system, and left to equilibrate for one week at ambient temperature. Daily measurements of the p-xylene NMR signal in the MOF sample using $\pi/2$ pulse NMR experiment were performed and showed no change in the signal over the course of the experiments. This ensured sorption equilibration had been reached before the start of our PFG-NMR measurements. A standard T_1 inversion recovery sequence was used to determine a T_1 time of 2.3 s. T_2 experiments were performed using a standard CPMG sequence with a delay time of 0.1 ms. The signal attenuation in the CPMG experiment showed two fractions of p-xylene which can be attributed to nearly all (91%) p-xylene inside the MOF ($T_2 = 2.2$ ms) and a small fraction (9%) in the interparticle space ($T_2 = 12$ ms).

Diffusion experiments were performed using a ^{1}H PFG-NMR 13-interval sequence with bipolar gradients and a longitudinal eddy-current delay of 6 ms.[10-12] The smallest gradient amplitude used in the measurements was chosen to be sufficiently large in order to fully attenuate any liquid or vapor phase p-xylene outside of the MOF channels. Typical parameters used were a diffusion time (t) of 160 ms, gradient durations (δ) of up to 1.5 ms, gradient amplitudes (g) of up to 19 T/m, and repetition delays around 4 s. Unusually large number of experiment repetitions (i.e. numbers of scans) of around 4000 had to be used for each gradient amplitude in order to generate reliable signal with acceptable signal-to-noise ratios (S/N). This was mostly related to low ^{1}H T_2 NMR relaxation time of p-xylene inside the MOF channels. The experimental uncertainty of the measured signal was determined by repeating the same measurements with an identical number of scans and comparing the data. Due to signal-to-noise limitations only an initial part of PFG-NMR attenuation curve could be measured.

The apparent self-diffusivity was estimated in the conventional way from the initial slope of the attenuation curve assuming normal 3D diffusion without diffusion anisotropy.[13, 14]

$$\Psi = \exp(-q^2 t D), \tag{4}$$

where Ψ is the PFG NMR signal attenuation, $q = 2\gamma g\delta$, and γ is the gyromagnetic ratio.

The measured PFG NMR attenuation data for p-xylene are shown in Fig. S8 Least square fit of these data by Eq. 4 resulted in the self-diffusion coefficient of $(8 \pm 4) \times 10^{-10}$ cm^{2}s^{-1} with the corresponding root mean square displacement of 0.27 ± 0.06 µm at 296 K. Large experimental uncertainty prevented us from making any conclusions about diffusion anisotropy and/or deviations from normal diffusion regime in the studied MOF. Long and short gradient pulse durations which altered the time intervals of the sequence[10] were used as a way to verify that changing the sequence parameters would not result in changes in the measured self-diffusivity, within uncertainty.

Liquid-Phase Xylene Coadsorption Experiments

The stock solutions for binary PX/OX coadsorption experiments were composed of 1,3,5-triisopropylbenzene (10 g, 48.9 mmol), PX (146 µL, 1.19 mmol), OX (143 µL, 1.19 mmol), and 1,3,5-tri-*tert*-buytlbenzene (293 mg, 1.19 mmol). The composition of the stock solutions for ternary PX/OX/MX coadsorption experiments was the same as that for binary PX/OX coadsorption experiment except that MX (146 µL, 1.19 mmol) was also added.

Zn(purine)I powder was activated at 200 °C under dynamic vacuum for 12 h. In a 2 mL scintillation vial, activated Zn(purine)I (25 mg) was dispersed in 1.4 mL stock solution (1.6 mL for UiO-66 experiments), and the dispersion was vigorously agitated along the experiments. About 1 mL

dispersion was sampled at pre-determined moments, and powder in the dispersion was removed by PTFE filters (0.45 μm). The compositions of particle-free samples were analyzed by a gas chromatography (7890 GC, Agilent) using an FID.
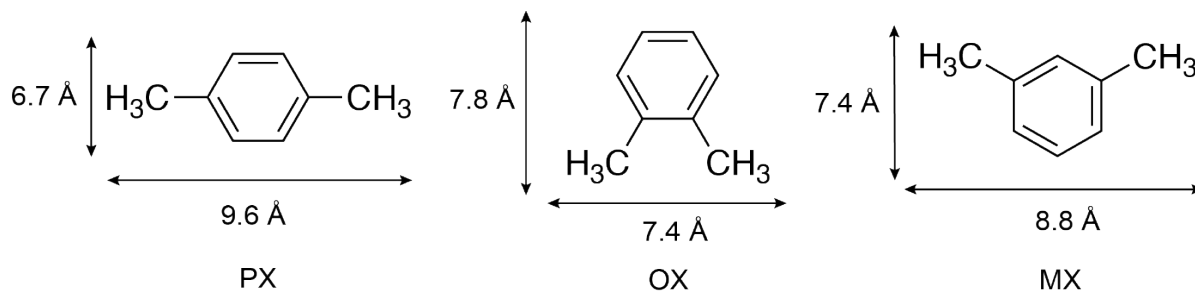
Scheme S1. Comparison of the dimensions of different xylene isomers.[15]
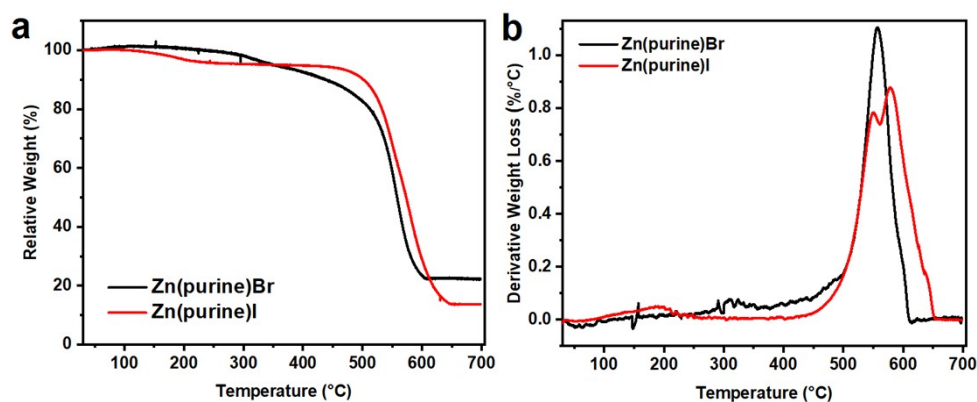
Fig. S1 TGA (a) and DTA (b) profiles of Zn(purine)Br (black) and Zn(purine)I (red) prior to 200 °C heat activation. The weight loss step at ~200°C suggested that solvent is still present in the MOF in the absence of high temperature activation.
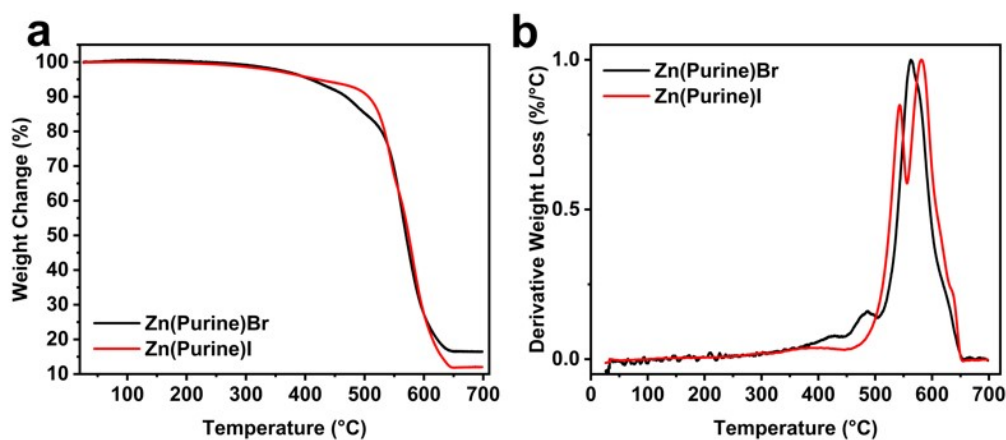
Fig. S2 TGA (a) and DTA (b) profiles of Zn(purine)Br (black) and Zn(purine)I (red) after activation at 200 °C. The DTA curves suggested that solvent molecules have been sufficiently removed after heat activation.

11
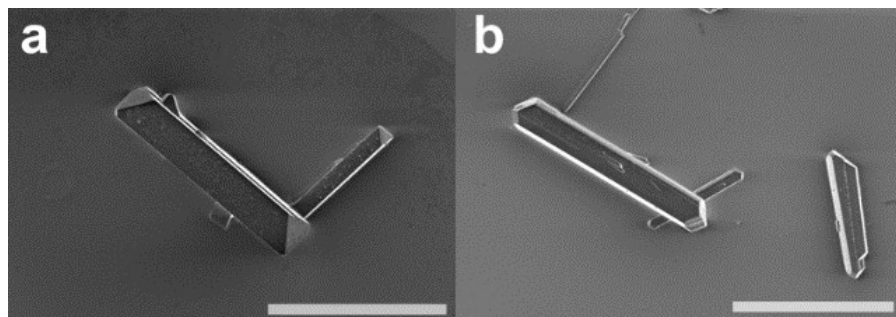
Fig. S3 SEM images of Zn(purine)Br (a) and Zn(purine)I (b). Scale bars are 50 μm.
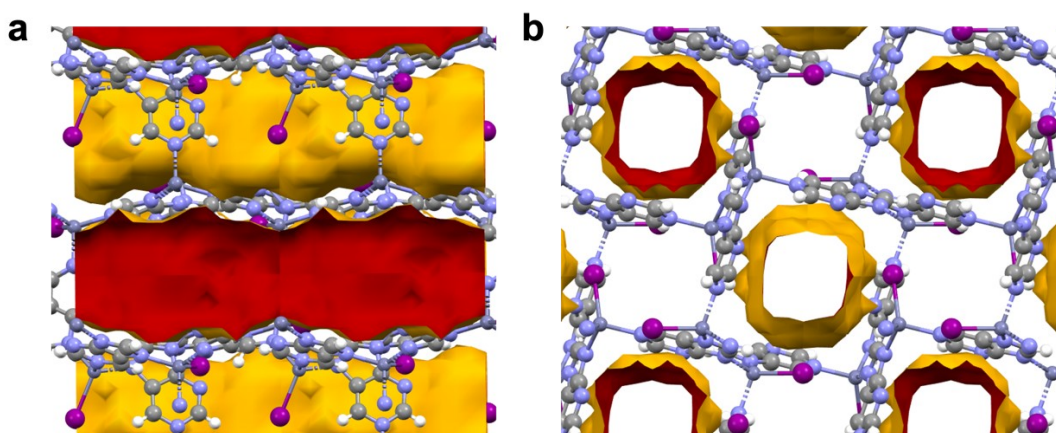
Fig. S4 Pore shape and accessible volumes indicated by yellow surfaces of Zn(purine)I viewed along the (a) b- and (b) a-axis using a probe radius of 1.2 Å (red surfaces represent the cross-section of the pores). Continuous 1D channels can be seen along the b-axis allowing the passage of guest molecules. C, grey; N, blue; Zn, dark grey; H, white; I, purple.
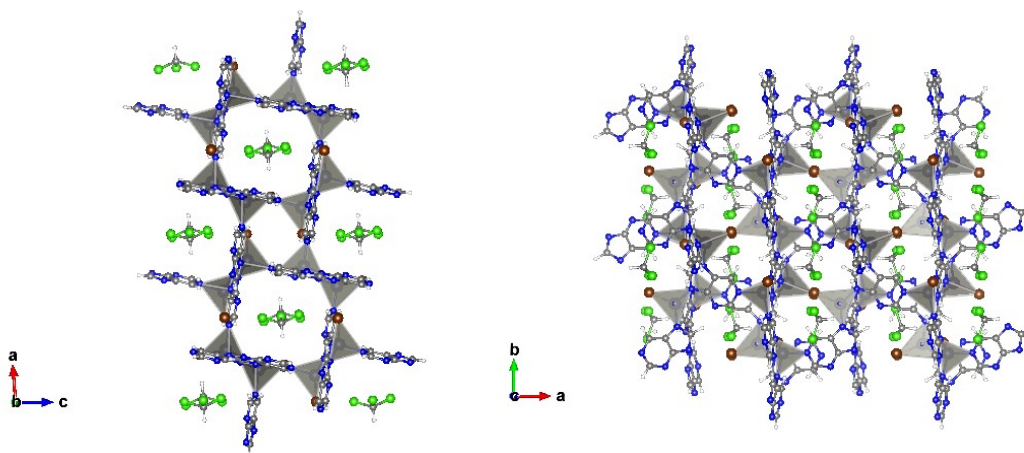
Fig. S5 Models of confined $CHCl_3$ solvent molecules within the void space of a Zn(purine)Br MOF lattice viewed down the b-axis (left) and c-axis (right). The size of the guest when compared to the size of the channel is a source of limited activation.
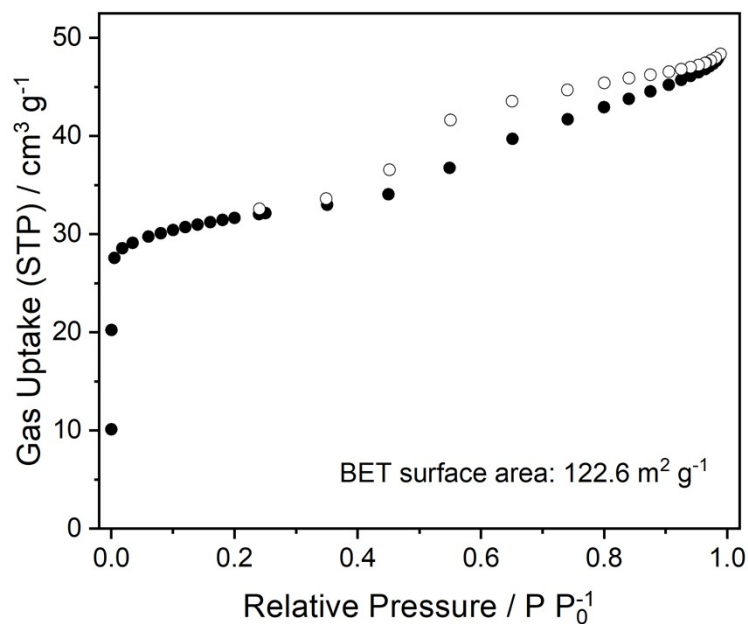
Fig. S6 N_2 adsorption (closed symbols) and desorption (open symbols) isotherms of Zn(purine)I at 77 K.
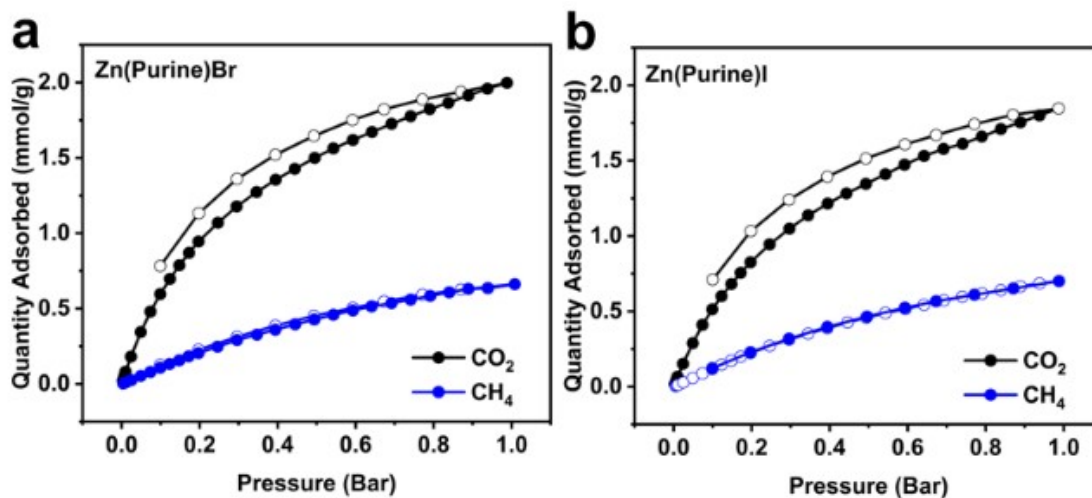
Fig. S7 Single component CO_2 (black) and CH_4 (blue) adsorption (closed symbols) and desorption (open symbols) isotherms of (a) Zn(purine)Br and (b) Zn(purine)I at 298 K.
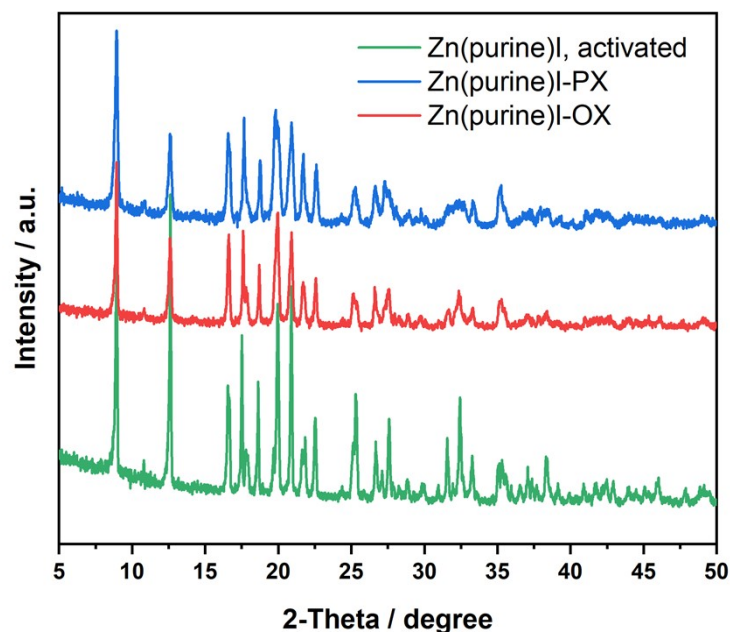
Fig. S8 The PXRD patterns of Zn(purine)I after activation and exposure to the vapor of xylene isomers.
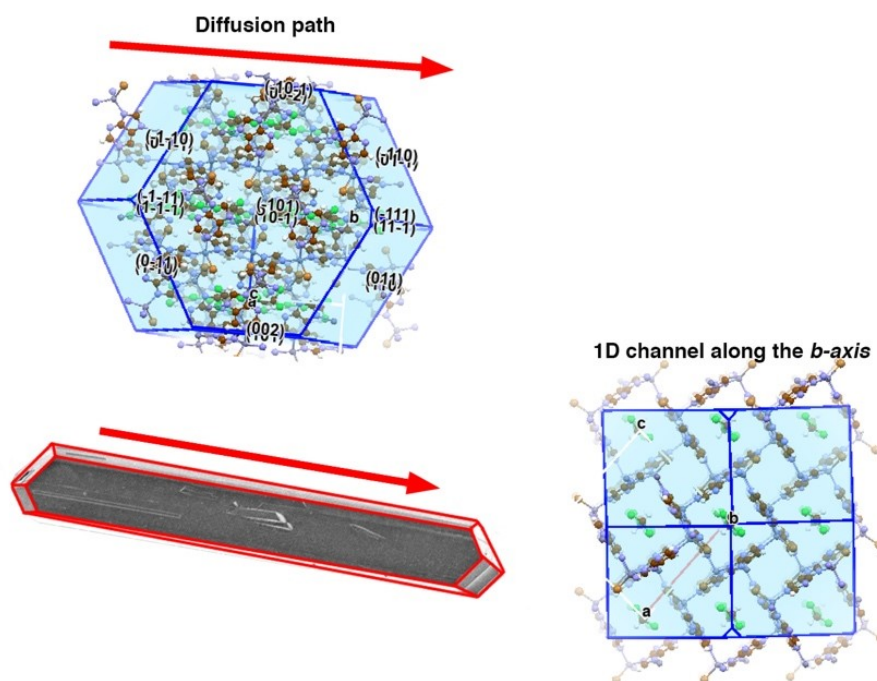
Fig. S9 Simulated crystal morphology and an SEM image of Zn(purine)Br with crystallographic faces and axes labeled. The *b*-axis (main diffusion path) is along the longest dimension of the crystals. BFDH method is applied for crystal morphology simulation using the Mercury software. The lattice parameters and atomic coordinates used in the model were obtained from experimentally determined single crystal data.
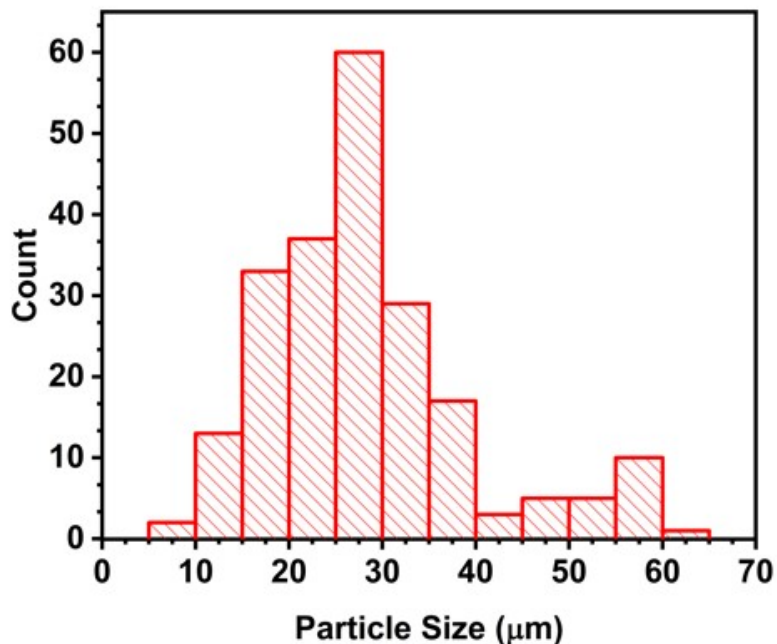
Fig. S10 Particle size distribution of Zn(purine)I used to calculate the xylene diffusivity values.
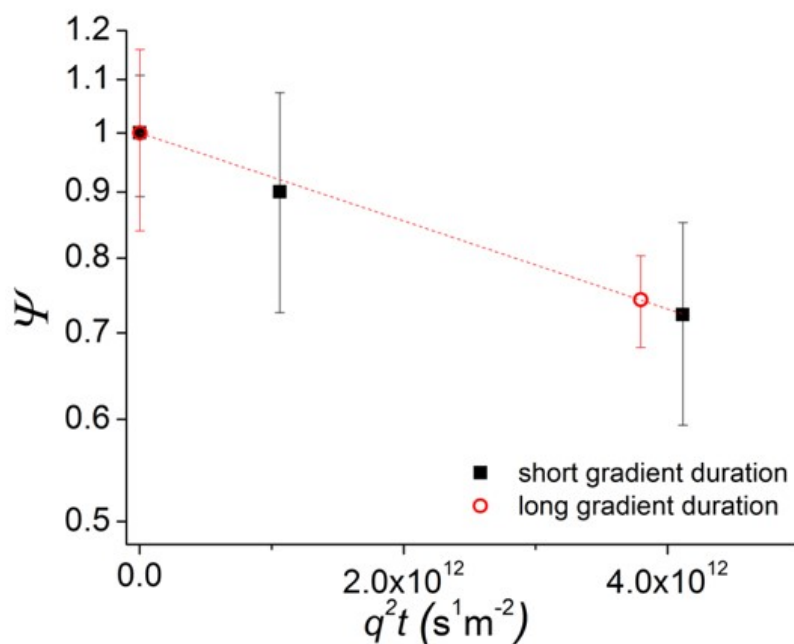
Fig. S11 ^{1}H PFG-NMR attenuation plot of *p*-xylene in Zn(purine)I MOF at 296 K. All measurements had a diffusion time of 160 ms and were averaged over 2 (red symbols) or 3 (black symbols) identical experiments. Black squares and red circles represent gradient durations of 1 ms and 1.5 ms respectively. Error bars represent one standard deviation interval. The red dashed line shows the monoexponential attenuation fit using Eq. 4.
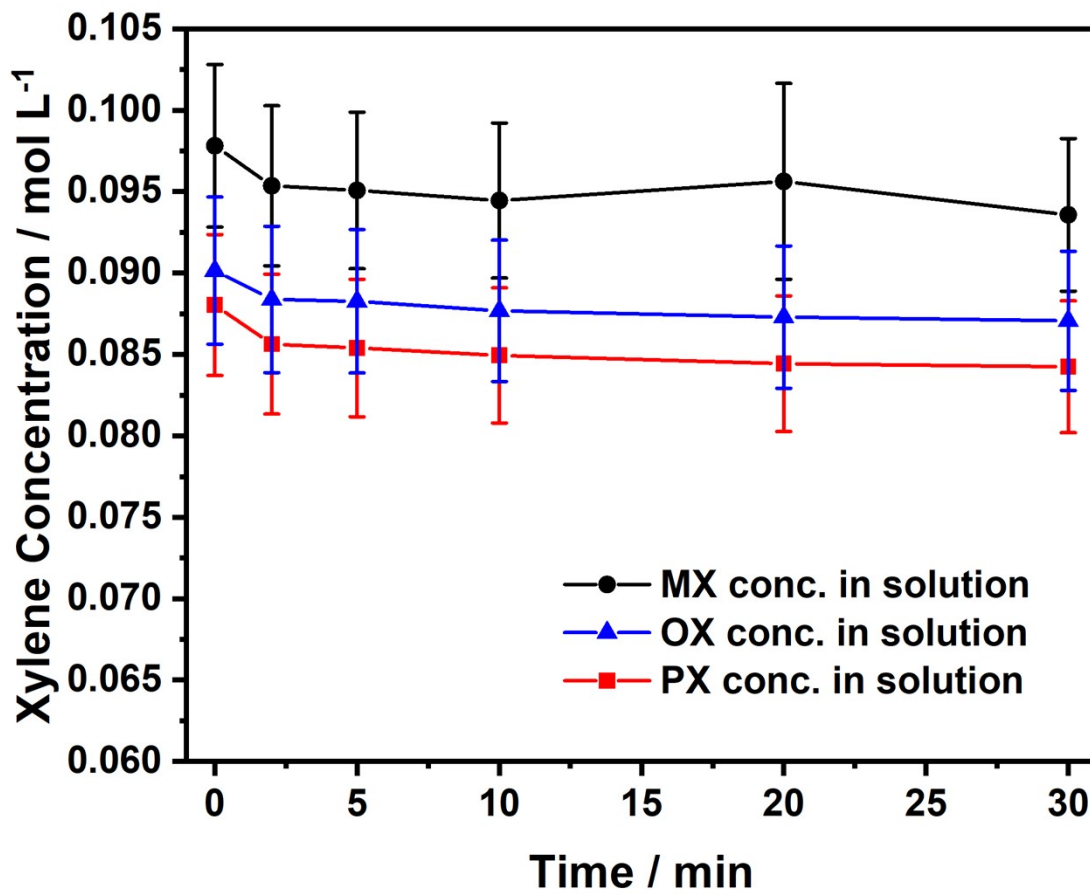
Fig. S12 Time-dependent liquid-phase concentrations of xylene isomers (PX, OX, and MX) in coadsorption experiments in TIPB using UiO-66 at room temperature.
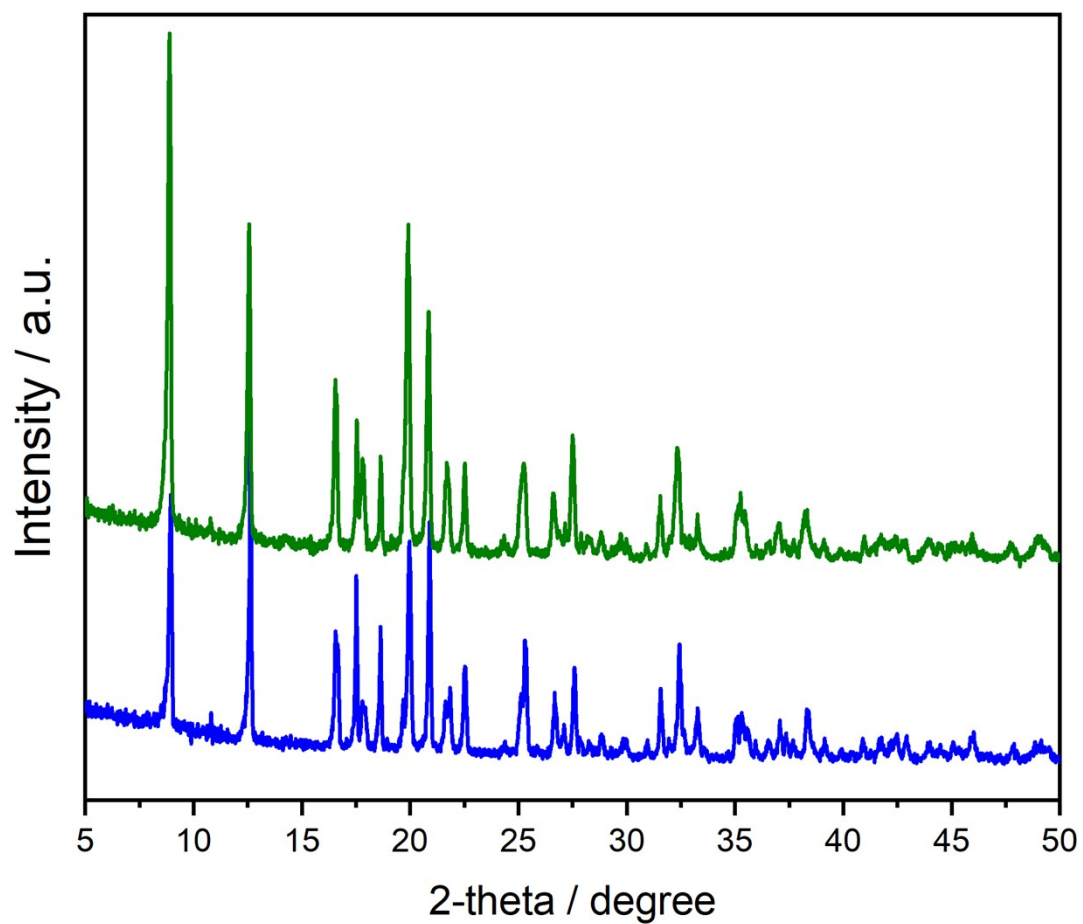
Fig. S13 PXRD patterns of Zn(purine)I before (blue) and after (green) liquid-phase xylene sorption experiments.

Table S1. Crystallographic parameters of RS8D3 and RS10D1

Identification code	**RS8D3**	**RS10D1**
Empirical formula	$C_{10}H_6Br_2N_8Zn_2$	$C_{10}H_6I_2N_8Zn_2$
Formula weight	528.79	622.77
Temperature/K	100.0	100.0
Crystal system	monoclinic	monoclinic
Space group	$P2_1/n$	$P2_1/n$
a/Å	13.8144(7)	14.0372(18)
b/Å	10.1970(5)	10.1884(13)
c/Å	13.8537(7)	14.0589(19)
α/°	90	90
β/°	91.3260(10)	92.057(3)
γ/°	90	90
Volume/Å^3	1950.99(17)	2009.4(5)
Z	4	4
ρ_{calc}g/cm^3	1.800	2.059
μ/mm^{-1}	1.509	1.247
F(000)	1008.0	1152.0
Crystal size/mm^3	0.06512 × 0.02671 × 0.0239	0.02242 × 0.02144 × 0.01567
Radiation	synchrotron (λ = 0.41328)	synchrotron (λ = 0.41328)
2Θ range for data collection/°	2.394 to 34.398	2.342 to 29.98
Index ranges	$-19 \leq h \leq 19, -14 \leq k \leq 14, -18 \leq l \leq 19$	$-17 \leq h \leq 17, -12 \leq k \leq 12, -17 \leq l \leq 17$
Reflections collected	57752	47951
Independent reflections	5844 [R_{int} = 0.0368, R_{sigma} = 0.0192]	4130 [R_{int} = 0.1337, R_{sigma} = 0.0597]
Data/restraints/parameters	5844/0/199	4130/0/199
Goodness-of-fit on F^2	1.112	1.118
Final R indexes [I>=2σ (I)]	R_1 = 0.0322, wR_2 = 0.0718	R_1 = 0.0789, wR_2 = 0.1968
Final R indexes [all data]	R_1 = 0.0389, wR_2 = 0.0776	R_1 = 0.0983, wR_2 = 0.2071
Largest diff. peak/hole / e Å^{-3}	1.32/-1.31	1.98/-2.21

Table S2. Comparison between unit cell parameters from XRD and DFT, with angles in degrees and distances in Å.

	α		β		γ		a		b		c	
	DFT	XRD	DFT	XRD	DFT	XRD	DFT	XRD	DFT	XRD	DFT	XRD
Zn(purine)Br	90.0	90.0	90.8	91.3	90.0	90.0	13.9	13.8	10.2	10.2	13.9	13.9
Zn(purine)I	90.0	90.0	91.6	92.1	90.0	90.0	14.1	14.0	10.2	10.2	14.1	14.1

Comparisons of Simulated Surface Area and Experimental Surface Area

The experimental BET surface areas was found to be 142 m^2/g for Zn(purine)Br and 130 m^2/g for Zn(purine)I, while the simulated surface areas are 391 m^2/g for Zn(purine)Br and 329 m^2/g for Zn(purine)I. Although incomplete removal of residual solvent inside a framework can result in an experimental surface area being smaller than expected for a solvent-free structure, our DFT calculations suggested that the binding energy of the solvent is quite low. Thus, we conducted further simulations to explore other possible reasons causing the surface area difference.

We first simulated single component isotherms of CH_4 and CO_2. If solvents are not completely removed in the experimental structure, we would expect the simulated isotherms to show considerably higher loadings than the experimental isotherms. Simulations with rigid MOF structures were performed with methods similar to earlier studies.[16] The DFT-minimized structures described above were used. Previous benchmarking calculations have indicated that this approach gives results in good agreement with solvent-free experimental structures.[17] Point charges for MOF atoms are calculated using DDEC6.[18] Simulations of single-component adsorption with fixed frameworks were performed using GCMC simulations with RASPA.[19] In these GCMC simulations, the van der Waals (vdW) interactions between adsorbates were described by the TraPPE[20] force field, and Lorentz-Berthelot mixing rules were used to define adsorbate-MOF interactions with the vdW parameters for MOF atoms given by the UFF4MOF.[21, 22] Truncated potentials with tail corrections were applied with Lennard-Jones interactions truncated at 12 Å. For CO_2, Coulombic interactions were modeled pairwise with a long-range Ewald summation scheme with an accuracy of 10^{-6}. Simulation volumes were expanded to at least 24 Å along each dimension and triclinic periodic boundary conditions were defined in all dimensions. Random Monte Carlo moves allowing for translation, rotation, regrowth, reinsertion, deletion, and insertion moves with equal probabilities were used for GCMC. Specifically, 105 MC cycles were used at each condition, and initial tests indicated this choice gave well-converged results.

To test whether flexibility of the MOF could have a strong influence on adsorption, sorption-relaxation simulations were performed at 300 K with a combined GCMC and MD technique in TAXI package.[23] UFF4MOF[21, 22] was used to describe both intraframework and framework-adsorbate interaction. The FF relaxed structure has a less than 3% difference compared to the DFT relaxed structure. Sorption–relaxation is carried out in multiple GCMC/MD iterations, where GCMC simulations are used to predict adsorbate loading and MD simulations are employed to

account for system rearrangement. Each GCMC portion of the sorption-relaxation approach was performed using RASPA for 105 cycles, which has the same setting as in the adsorption simulations defined above. MD simulations were carried out with the LAMMPS software package 1 ns with barostat conditions corresponding to the adsorbate's bulk phase pressure and thermostat conditions corresponding to isotherm temperature. During the MD process, both atom positions and the unit cell dimensions were allowed to change. This iterative process was repeated until an equilibrium is reached.

The simulated isotherms are compared to experimental data in Fig. S12. There are only small differences between the simulations with rigid and flexible structures. Including MOF flexibility would be important if simulations were being used to make high precision predictions, but for our purposes it is clear that the rigid calculations are sufficient to make useful comparisons with experimental data. Simulated CO_2 isotherms have lower loadings than the experimental data, while the CH_4 isotherms show the opposite deviation with respect to experiment. If the lower measured surface area of the MOFs relative to the solvent-free structure was due to pore blockage by residual solvent, the simulated CO_2 and CH_4 isotherms would be expected to both show significantly larger loadings than the experiments. We therefore ascribe the difference between simulated isotherms and experimental isotherms to the inaccuracy of the generic force field used in our calculations. Similar discrepancies have been seen in previous systematic comparisons between simulations of this kind and replicate experimental studies of CO_2 adsorption.[24]
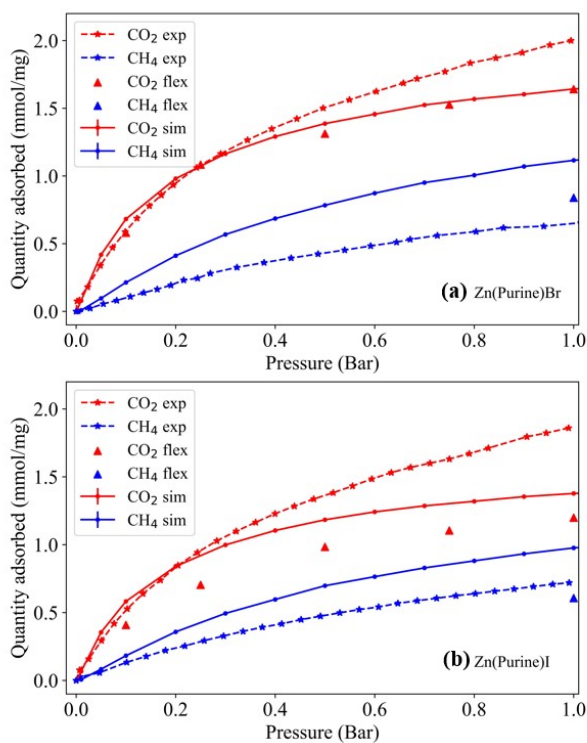
Fig. S14 CO_2 and CH_4 adsorption isotherms in (a) Zn(purine)Br, (b) Zn(purine)I. Dashed lines are experimental isotherms. Solid lines show simulation results using rigid MOF structures and the triangles are results from sorption-relaxation calculations with a fully flexible MOF.

Table S3. Crystal dimension data of Zn(purine)I for the calculation of particle size distribution.

No.	Length / μm	Width / μm	No.	Length / μm	Width / μm	No.	Length / μm	Width / μm	No.	Length / μm	Width / μm
1	20.215	7.213	37	56.932	8.002	73	27.455	8.632	109	16.939	8.113
2	15.155	3.689	38	26.435	7.847	74	18.121	5.264	110	30.298	6.471
3	17.695	4.473	39	15.088	6.355	75	33.462	4.888	111	28.81	6.452
4	36.432	7.463	40	56.044	9.151	76	18.992	7.708	112	15.266	3.311
5	30.547	2.679	41	31.616	9.665	77	51.247	5.493	113	17.743	7.247
6	13.627	1.794	42	34.629	9.265	78	28.074	7.644	114	35.49	7.11
7	25.4	4.505	43	27.894	7.917	79	61.663	5.658	115	23.962	7.369
8	12.985	4.45	44	31.097	8.667	80	24.694	7.483	116	26.846	4.009
9	32.589	6.804	45	36.567	9.211	81	27.727	7.936	117	18.932	6.528
10	20.159	5.484	46	30.138	9.832	82	12.055	6.208	118	9.393	6.208
11	31.763	6.182	47	26.965	7.005	83	20.479	6.724	119	28.172	7.369
12	20.695	3.925	48	21.491	8.113	84	18.802	8.082	120	17.199	7.448
13	32.348	7.886	49	16.672	2.73	85	27.681	8.779	121	29.336	9.032
14	20.444	5.756	50	26.753	8.885	86	34.615	7.314	122	22.4	8.451
15	30.85	4.715	51	21.582	7.365	87	38.458	9.578	123	55.62	8.77
16	34.237	9.882	52	30.522	6.814	88	54.816	8.741	124	19.664	5.898
17	34.562	10.943	53	27.464	5.234	89	29.686	10.366	125	21.186	7.213
18	30.734	7.696	54	10.366	7.213	90	32.994	7.302	126	23.541	6.471
19	26.662	10.231	55	8.681	6.043	91	13.112	8.614	127	25.462	3.755
20	37.55	6.058	56	40.218	7.213	92	37.113	5.234	128	31.08	6.144
21	23.231	6.129	57	19.814	5.669	93	23.646	3.456	129	55.122	10.327
22	26.027	9.498	58	26.3	7.053	94	25.598	4.334	130	27.802	8.685
23	31.763	9.235	59	30.565	2.741	95	31.666	9.879	131	29.407	4.963
24	26.107	10.183	60	26.321	5.707	96	37.406	8.556	132	28.433	7.835
25	31.658	7.465	61	15.482	3.235	97	28.973	7.547	133	23.529	6.681
26	20.308	6.899	62	22.691	3.509	98	36.066	5.626	134	17.934	4.994
27	29.983	9.11	63	22.484	7.752	99	11.77	2.456	135	26.307	6.002
28	35.176	8.396	64	19.157	8.545	100	48.339	5.904	136	43.127	5.898
29	23.268	5.549	65	26.81	10.137	101	17.962	5.794	137	36.309	10.533
30	20.349	5.357	66	19.655	6.607	102	10.507	3.17	138	13.904	7.378
31	23.554	5.598	67	32.07	10.003	103	14.23	4.029	139	28.5	9.327
32	24.526	11.067	68	30.819	9.69	104	25.088	8.969	140	29.51	9.032
33	24.399	6.223	69	27.552	7.752	105	36.757	7.577	141	22.682	10.433
34	48.941	6.992	70	29.049	8.282	106	49.496	11.599	142	16.326	2.555
35	18.762	4.397	71	19.211	6.452	107	37.59	5.091	143	56.713	8.002
36	20.92	2.591	72	49.931	7.298	108	26.172	5.276	144	25.598	11.152

Table S3 (continued)

No.	Length / μm	Width / μm	No.	Length / μm	Width / μm	No.	Length / μm	Width / μm	No.	Length / μm	Width / μm
145	25.291	5.809	163	11.791	6.456	181	24.007	7.788	199	23.874	6.668
146	20.356	6.223	164	39.906	5.061	182	56.891	11.21	200	52.714	9.231
147	19.68	7.704	165	17.093	6.677	183	27.646	7.792	201	28.956	8.341
148	28.425	8.14	166	25.331	5.549	184	26.435	9.104	202	31.979	10.437
149	22.56	6.452	167	18.979	5.018	185	59.039	9.501	203	16.775	6.103
150	42.35	6.658	168	25.31	6.621	186	26.172	5.091	204	19.921	6.263
151	18.31	6.827	169	26.059	6.248	187	23.125	3.264	205	33.58	7.302
152	27.048	7.448	170	29.391	5.442	188	56.016	11.363	206	22.449	5.883
153	37.901	8.812	171	27.619	5.729	189	38.794	11.366	207	32.332	10.69
154	36.092	7.053	172	17.109	4.218	190	20.787	7.644	208	29.914	8.128
155	45.215	5.115	173	50.105	8.863	191	29.583	8.249	209	27.407	8.646
156	56.889	10.365	174	12.458	5.794	192	56.153	9.546	210	29.281	7.982
157	35.808	8.437	175	28.04	6.233	193	32.717	4.494	211	25.408	8.663
158	15.545	7.696	176	22.476	4.517	194	26.411	6.404	212	51.69	7.14
159	20.737	4.009	177	13.623	4.651	195	26.078	6.551	213	22.66	8.925
160	15.046	6.277	178	16.942	7.677	196	21.452	6.556	214	33.084	10.687
161	27.977	9.68	179	18.11	6.605	197	11.874	6.103	215	20.805	8.966
162	28.224	10.258	180	26.243	4.875	198	25.315	9.184			

Table S4 Comparison of xylene separation performance of selected zeolites and MOFs.

Adsorbents	Xylene Uptakes / mmol g^{-1}			Temperature /	Selectivity		Methods of determining	Ref
	PX	OX	MX	K	PX/OX	PX/MX	selectivity	
Zn(purine)I	0.51 (x_{PX} = 0.02)	N.A.	N.A.	298	N.A.*	N.A.*	Liquid-phase batch coadsorption in tri-isopropyl benzene	This work
BaX	0.97 (50 wt% in isooctane)	0.45 (50 wt% in isooctane)	0.19 (50 wt% in isooctane)	423	2.82	7.19	Liquid-phase breakthrough experiments	25
H/ZSM-5	1.3 (45 wt% in isooctane)	0.29 (45 wt% in isooctane)	0.12 (45 wt% in isooctane)	N.A.	16.8	25.0	Liquid-phase breakthrough experiments	26
NaY	0.42 (45 wt% in isooctane)	0.40 (45 wt% in isooctane)	1.0 (45 wt% in isooctane)	403	N.A.	0.38	Liquid-phase breakthrough experiments in isooctane	27
UiO-66	0.28 (P_{PX} = 2.5 kPa)	0.81 (P_{OX} = 2.5 kPa)	0.46 (P_{MX} = 2.5 kPa)	398	0.36	0.61	Vapor-phase breakthrough experiments	28
UiO-66	3.04 (C_{PX} = 2.68 mol/kg)	3.51 (C_{OX} = 2.72 mol/kg)	-	313	0.42	0.91	Liquid-phase breakthrough experiments in n-heptane	29
MIL-53(Al)	0.49 (x_{PX} = 0.22)	3.0 (x_{OX} = 0.22)	1.0 (x_{MX} = 0.44)	323	0.19	0.98	Liquid-phase breakthrough experiments	30
Ce(HTCPB)	0.85n (x_{PX} = 0.5)	0.15 (x_{OX} 0.5)	0.18 (x_{MX} = 0.5)	383	5.7	4.6	Liquid-phase batch coadsorption	31
CD-MOF-2	2.5 (P_{PX} = 0.81 mbar)	1.1 (P_{OX} = 0.80 mbar)	1.4 (P_{MX} = 0.80 mbar)	333	0.06	0.29	Vapor-phase breakthrough experiments	32
Guest-free MAF-36	N.A.	N.A.	N.A.	298	50	48.9	Liquid-phase batch coadsorption	33
Ni(NCS)$_2$(ppp)$_4$	N.A.	N.A.	N.A.	295	0.025	0.59	Vapor-phase batch coadsorption	34
AgLClO$_4$	1.2 (x_{PX} = 0.5)	0.033 (x_{OX} = 0.5)	0.2 (x_{MX} = 0.5)	383	24.0	6.19	Liquid-phase batch coadsorption	35
[Zn$_2$(aip)$_2$(bpy)]	1.7 (P/P$_0$ = 0.99)	1.6 (P/P$_0$ = 0.99)	0.95 (P/P$_0$ = 0.99)	298	16.0	5.0	Liquid-phase batch coadsorption	36
FePzNi	1.8 (P/P$_0$ = 0.99)	0.22 (P/P$_0$ = 0.99)	0.45 (P/P$_0$ = 0.99)	298	2	MX-selectiv	Vapor-phase coadsorption	37

						e		
Co$_2$(dobdc)	0.34 (C_{PX} = 1.0 M in heptane)	0.91 (C_{OX} = 0.91 M in heptane)	0.44 (C_{MX} = 1.0 M in heptane)	306	0.26	0.63	Liquid-phase coadsorption in heptane	38
sql-1-Co-NCS	8.0 (P/P$_0$ = 0.99)	8.0 (P/P$_0$ = 0.99)	7.8 (P/P$_0$ = 0.99)	298	0.10	0.77	Liquid-phase batch coadsorption	39
ZU-61	3.4 (P_{PX} = 7 mbar)	N.A.	3.4 (P_{MX} = 7 mbar)	333	N.A.	0.34	Vapor-phase breakthrough experiments	40
NU-2000	1.1 (x_{PX} = 0.33)	0.06 (x_{OX} = 0.33)	0.29 (x_{MX} = 0.33)	298	20	3.9	Liquid-phase batch coadsorption	41
Cu(CDC)	1.1 (C_{PX} = 0.48 M in mesitylene)	0.09 (C_{OX} = 0.49 M in mesitylene)	0.0.16 (C_{MX} = 0.49 M in mesitylene)	298	10	7	Liquid-phase batch coadsorption in mesitylene	42
DUT-8(Cu)	1.9 (C_{PX} = 0.37 M in isooctane)	0.40 (C_{OX} = 0.39 M in isooctane)	0.29 (C_{OX} = 0.39 M in isooctane)	298	5.4	7.2	Liquid-phase batch coadsorption in isooctane	43
MFM-300(Fe)	1.7 (C_{PX} = 0.60 M in pentane)	12 (C_{OX} = 0.64 M in pentane)	18 (C_{MX} = 0.66 M in pentane)	293	0.36	0.26	Liquid-phase breakthrough experiments in pentane	44

* Negligible MX or OX uptakes were observed during the coadsorption experiments.

References

1. G. Kresse and D. Joubert, *Phys. Rev. B*, 1999, **59**, 1758-1775.
2. P. E. Blöchl, *Phys. Rev. B*, 1994, **50**, 17953-17979.
3. K. Lee, E. D. Murray, L. Kong, B. I. Lundqvist and D. C. Langreth, *Phys. Rev. B*, 2010, **82**.
4. J. P. Perdew, K. Burke and M. Ernzerhof, *Phys. Rev. Lett.*, 1996, **77**, 3865-3868.
5. S. Grimme, J. Antony, S. Ehrlich and H. Krieg, *J. Chem. Phys.*, 2010, **132**.
6. T. F. Willems, C. H. Rycroft, M. Kazi, J. C. Meza and M. Haranczyk, *Microporous Mesoporous Mat.*, 2012, **149**, 134-141.
7. Y. G. Chung, J. Camp, M. Haranczyk, B. J. Sikora, W. Bury, V. Krungleviciute, T. Yildirim, O. K. Farha, D. S. Sholl and R. Q. Snurr, *Chem. Mater.*, 2014, **26**, 6185-6192.
8. J. Crank, *The mathematics of diffusion*, Clarendon Press, Oxford, Eng, 2d edn., 1975.
9. C. Zhang, R. P. Lively, K. Zhang, J. R. Johnson, O. Karvan and W. J. Koros, *J. Phys. Chem. Lett.*, 2012, **3**, 2130-2134.
10. P. Galvosas, F. Stallmach, G. Seiffert, J. Kärger, U. Kaess and G. Majer, *J. Magn. Reson.*, 2001, **151**, 260-268.
11. R. M. Cotts, M. J. R. Hoch, T. Sun and J. T. Markert, *J. Magn. Reson. (1969)*, 1989, **83**, 252-266.
12. S. J. Gibbs and C. S. Johnson, *J. Magn. Reson. (1969)*, 1991, **93**, 395-402.
13. S. Berens, F. Hillman, H.-K. Jeong and S. Vasenkov, *Microporous Mesoporous Mat.*, 2019, **288**, 109603.
14. J. Kärger, D. M. Ruthven and D. N. Theodorou, *Diffusion in Nanoporous Materials, 2 Volume Set*, John Wiley & Sons, 2012.
15. Z. Qiao, Y. Yan, Y. Tang, H. Liang and J. Jiang, *J. Phys. Chem. C*, 2021, **125**, 7839-7848.
16. D. Tang, Y. Wu, R. J. Verploegh and D. S. Sholl, *ChemSusChem*, 2018, **11**, 1567-1575.
17. D. Nazarian, P. Ganesh and D. S. Sholl, *J. Mater. Chem. A*, 2015, **3**, 22432-22440.
18. T. A. Manz and D. S. Sholl, *J. Chem. Theory Comput.*, 2010, **6**, 2455-2468.
19. D. Dubbeldam, S. Calero, D. E. Ellis and R. Q. Snurr, *Mol. Simul.*, 2016, **42**, 81-101.
20. C. D. Wick, M. G. Martin and J. I. Siepmann, *J. Phys. Chem. B*, 2000, **104**, 8008-8016.
21. D. E. Coupry, M. A. Addicoat and T. Heine, *J. Chem. Theory Comput.*, 2016, **12**, 5215-5225.
22. A. K. Rappe, C. J. Casewit, K. S. Colwell, W. A. Goddard and W. M. Skiff, *J. Am. Chem. Soc.*, 1992, **114**, 10024-10035.
23. D. M. Anstine, D. Tang, D. S. Sholl and C. M. Colina, *NPJ Comput. Mater.*, 2021, **7**, 53.
24. J. Park, J. D. Howe and D. S. Sholl, *Chem. Mater.*, 2017, **29**, 10487-10495.
25. M. Rasouli, N. Yaghobi, F. Allahgholipour and H. Atashi, *Chem. Eng. Res. Des.*, 2014, **92**, 1192-1199.
26. M. Rasouli, N. Yaghobi, S. Chitsazan and M. H. Sayyar, *Microporous Mesoporous Mat.*, 2012, **150**, 47-54.
27. M. Rasouli, N. Yaghobi, S. Chitsazan and M. H. Sayyar, *Microporous Mesoporous Mat.*, 2012, **152**, 141-147.
28. P. S. Bárcia, D. Guimarães, P. A. P. Mendes, J. A. C. Silva, V. Guillerm, H. Chevreau, C. Serre and A. E. Rodrigues, *Microporous Mesoporous Mat.*, 2011, **139**, 67-73.
29. M. A. Moreira, J. C. Santos, A. F. P. Ferreira, J. M. Loureiro, F. Ragon, P. Horcajada, K.-E. Shim, Y.-K. Hwang, U. H. Lee, J.-S. Chang, C. Serre and A. E. Rodrigues, *Langmuir*, 2012, **28**, 5715-5723.

30. M. Agrawal, S. Bhattacharyya, Y. Huang, K. C. Jayachandrababu, C. R. Murdock, J. A. Bentley, A. Rivas-Cardona, M. M. Mertens, K. S. Walton, D. S. Sholl and S. Nair, *J. Phys. Chem. C*, 2018, **122**, 386-397.

31. J. E. Warren, C. G. Perkins, K. E. Jelfs, P. Boldrin, P. A. Chater, G. J. Miller, T. D. Manning, M. E. Briggs, K. C. Stylianou, J. B. Claridge and M. J. Rosseinsky, *Angew. Chem., Int. Ed.*, 2014, **53**, 4592-4596.

32. J. M. Holcroft, K. J. Hartlieb, P. Z. Moghadam, J. G. Bell, G. Barin, D. P. Ferris, E. D. Bloch, M. M. Algaradah, M. S. Nassar, Y. Y. Botros, K. M. Thomas, J. R. Long, R. Q. Snurr and J. F. Stoddart, *J. Am. Chem. Soc.*, 2015, **137**, 5706-5719.

33. X. Yang, H.-L. Zhou, C.-T. He, Z.-W. Mo, J.-W. Ye, X.-M. Chen and J.-P. Zhang, *Research*, 2019, **2019**, 9463719.

34. M. Lusi and L. J. Barbour, *Angew. Chem., Int. Ed.*, 2012, **51**, 3928-3931.

35. N. Sun, S. Q. Wang, R. Q. Zou, W. G. Cui, A. Q. Zhang, T. Z. Zhang, Q. Li, Z. Z. Zhuang, Y. H. Zhang, J. L. Xu, M. J. Zaworotko and X. H. Bu, *Chem. Sci.*, 2019, **10**, 8850-8854.

36. J. Lee, Y. Kim, Y. Son, H. Kim, Y. Nam Choi, D. D'Alessandro, P. Chandra Rao and M. Yoon, *Chem. Eur. J.*, 2021, **27**, 14851-14857.

37. M. Shivanna, K.-i. Otake, J.-J. Zheng, S. Sakaki and S. Kitagawa, *Chem. Commun.*, 2020, **56**, 9632-9635.

38. M. I. Gonzalez, M. T. Kapelewski, E. D. Bloch, P. J. Milner, D. A. Reed, M. R. Hudson, J. A. Mason, G. Barin, C. M. Brown and J. R. Long, *J. Am. Chem. Soc.*, 2018, **140**, 3412-3422.

39. S. Q. Wang, S. Mukherjee, E. Patyk-Kazmierczak, S. Darwish, A. Bajpai, Q. Y. Yang and M. J. Zaworotko, *Angew. Chem. Int. Ed.*, 2019, **58**, 6630-6634.

40. X. Cui, Z. Niu, C. Shan, L. Yang, J. Hu, Q. Wang, P. C. Lan, Y. Li, L. Wojtas, S. Ma and H. Xing, *Nat. Commun.*, 2020, **11**, 5456.

41. K. B. Idrees, Z. Li, H. Xie, K. O. Kirlikovali, M. Kazem-Rostami, X. Wang, X. Wang, T.-Y. Tai, T. Islamoglu, J. F. Stoddart, R. Q. Snurr and O. K. Farha, *J. Am. Chem. Soc.*, 2022, **144**, 12212-12218.

42. J. Lannoeye, B. Van de Voorde, B. Bozbiyik, H. Reinsch, J. Denayer and D. De Vos, *Microporous Mesoporous Mat.*, 2016, **226**, 292-298.

43. S.-I. Kim, S. Lee, Y. G. Chung and Y.-S. Bae, *ACS Appl. Mater. Interfaces*, 2019, **11**, 31227-31236.

44. X. Li, J. Wang, N. Bai, X. Zhang, X. Han, I. da Silva, C. G. Morris, S. Xu, D. M. Wilary, Y. Sun, Y. Cheng, C. A. Murray, C. C. Tang, M. D. Frogley, G. Cinque, T. Lowe, H. Zhang, A. J. Ramirez-Cuesta, K. M. Thomas, L. W. Bolton, S. Yang and M. Schröder, *Nat. Commun.*, 2020, **11**, 4280.